Efficient fringe image enhancement based on dual-tree complex wavelet transform

Tai-Chiu Hsung, Daniel Pak-Kong Lun,* and William W.L. Ng

Centre for Signal Processing, Department of Electronic and Information Engineering, The Hong Kong Polytechnic University, Hong Kong, China

*Corresponding author: enpklun@polyu.edu.hk

Received 7 September 2010; revised 26 April 2011; accepted 24 May 2011; posted 3 June 2011 (Doc. ID 134405); published 14 July 2011

In optical phase shift profilometry (PSP), parallel fringe patterns are projected onto an object and the deformed fringes are captured using a digital camera. It is of particular interest in real time three-dimensional (3D) modeling applications because it enables 3D reconstruction using just a few image captures. When using this approach in a real life environment, however, the noise in the captured images can greatly affect the quality of the reconstructed 3D model. In this paper, a new image enhancement algorithm based on the oriented two-dimenional dual-tree complex wavelet transform (DT-CWT) is proposed for denoising the captured fringe images. The proposed algorithm makes use of the special analytic property of DT-CWT to obtain a sparse representation of the fringe image. Based on the sparse representation, a new iterative regularization procedure is applied for enhancing the noisy fringe image. The new approach introduces an additional preprocessing step to improve the initial guess of the iterative algorithm. Compared with the traditional image enhancement techniques, the proposed algorithm achieves a further improvement of 7.2 dB on average in the signal-to-noise ratio (SNR). When applying the proposed algorithm to optical PSP, the new approach enables the reconstruction of 3D models with improved accuracy from 6 to 20 dB in the SNR over the traditional approaches if the fringe images are noisy.

OCIS codes: 100.2650, 100.5070, 100.5088, 100.7410, 110.4280.

1. Introduction

Among various noncontact three-dimensional (3D) measurement technologies, phase shift profilometry (PSP) [1–4] is of particular interest because it can deliver the 3D model of an object using only a few image captures. Its applications include real time motion captures [1], quality control in printed circuit board manufacturing [2], intelligent robot control, and many others [3]. When using PSP in practical applications, the captured images are often contaminated by noise. This may be due to the practical limitations of the working environment and the imperfection of the optical devices. It is particularly the case when the technique is used in some real time applications where images are captured with a short exposure time. The noise problem in the captured images significantly reduces the robustness of the algorithm. It requires not only effective but also efficient measures to solve the problem since the whole operation is performed in real time.

The general system setup of the PSP is shown in Fig. 1. In the figure, parallel fringe patterns are projected from G onto an object (e.g., Fig. 2) and the deformed fringes are captured using a digital camera. The height of the object deforms the fringe pattern by introducing a phase shift [4], which can be formulated as

$$g(x,y) = r(x,y) + c(x,y)\cos[2\pi f_0 x + \phi(x,y)], \quad (1)$$

where $g(x,y)$ is the deformed fringe image, f_o is the fundamental frequency of the sinusoidal fringe pattern in the x direction, and $\phi(x,y)$ is the "absolute phase" to be estimated. Since it is in a

0003-6935/11/213973-14$15.00/0

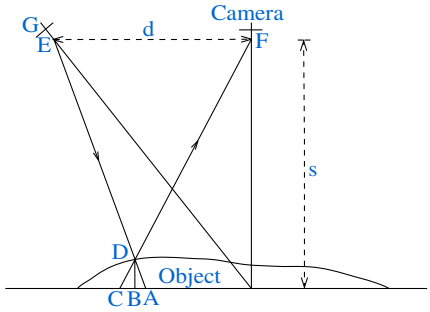

Fig. 1. (Color online) Setup for optical PSP.

two-dimensional (2D) form, we also call $\phi(x,y)$ the phase image. As can be seen in Eq. (1), $\phi(x,y)$ phase-modulates the cosine function, hence, its estimation can also be considered as a demodulation process applied to $g(x,y)$. If $\phi(x,y)$ is known, the height profile of the object can be readily obtained. Using s as the distance between the camera and a reference plane and d as the distance between the camera and the projector as shown in Fig. 1, the height of the object can be reconstructed from the phase by $h(x,y) = \phi(x,y) \cdot s/(2\pi f_0 d + \phi(x,y))$ [4]. In Eq. (1), $r(x,y)$ and $c(x,y)$ model the effects due to irregular reflectance of the object and transmission variations. $r(x,y)$ has to be removed from the images or a severe reconstruction error will result. To do so, the Fourier transform (FT) profilometry [3,4] and the wavelet transform profilometry [5–8] approaches were suggested for the demodulation process. Another commonly used approach is the π-shifted PSP [2] that captures two fringe images with a π phase shifted between the fringe patterns. By subtracting the second image from the first one, the resulting image will have $r(x,y)$ effectively removed. The demodulation process can then be directly carried out by applying the Hilbert transform to the resulting image.

The above-mentioned demodulation methods, however, have a common deficiency that only the wrapped phase $\hat{\phi}(x,y)$ can be obtained rather than the required absolute phase $\phi(x,y)$, which is related to the wrapped phase by $\phi(x,y) = \hat{\phi}(x,y) + 2M\pi$; M is an unknown integer. To obtain $\phi(x,y)$ from $\hat{\phi}(x,y)$, a phase unwrapping process is needed to estimate the unknown M. It is not trivial, particularly when the captured fringe images are noisy, and/or there are abrupt changes in object shape. Errors will be generated in the unwrapping process and, more importantly, the errors will propagate to other parts of the phase image such that the 3D model reconstructed based on that will have severe distortion. To deal with the problem, one research direction is to develop robust phase unwrapping methods. Examples include the path-following approaches [9] such as Goldstein's method and the minimization approaches such as that in [10]. Nevertheless, these approaches may either be too computationally intensive or not robust enough at high noise levels. Another direction is to directly denoise the estimated wrapped phase image [11–14]. However, the errors in the estimated wrapped phase image can hardly be modeled by a random process with known distribution. The denoising process can be rather complicated and may not be effective.

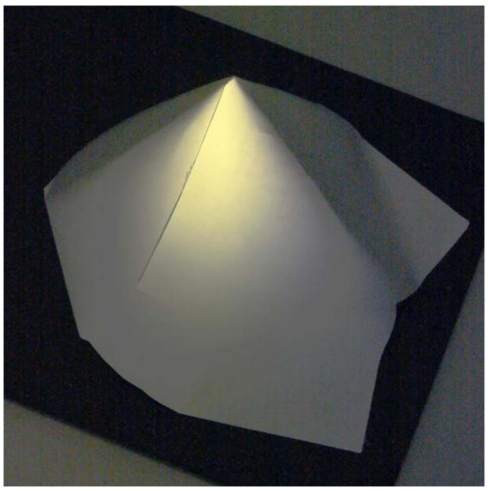

Fig. 2. (Color online) Test object.

In fact, the problem in phase unwrapping stems from the noisy fringe images in which the behavior of noise is rather well known. Enhancing these images should be more effective than enhancing the phase images. Earlier work in this direction includes [2], in which fast nonlinear one-dimensional (1D) filtering and 2D median filtering methods are adopted for suppressing noise in the image capturing process. In [15–19], a windowed FT (WFT) is suggested for the denoising and demodulation of the fringe images. The denoising is achieved by hard thresholding of the WFT transform coefficients and then applying the inverse WFT. The method is also known [15–19] as windowed Fourier filtering (WFF). Very promising results can be achieved provided that the threshold and the sampling frequency are selected appropriately. However, WFF is an extremely time-consuming process, which imposes great difficulty when applied to real time applications.

Recent advances in iterative regularization methods have added a new dimension to the study of image enhancement [20–24]. In these approaches, a sparse representation of the image is first obtained by transforming the image with basis functions that are compactly supported and have high vanishing moments. A typical example is the wavelet function. The enhancement of a noisy image can be modeled as an iterative optimization process. Although the technique is very effective in removing noise while preserving image edges, much difficulty arises when applying it to fringe image denoising. As opposed to normal images, fringe images do not have smooth regions but only fringes, which are indeed sinusoidal functions as given in Eq. (1). Traditional iterative regularization techniques that assume a sparse representation of the image can be obtained by transforming the image are not necessarily valid for fringe images. For instance, wavelet transforming

a sinusoidal function using the traditional Daubechies wavelet functions will never give a sparse representation. Since the transform coefficients are not sparse, it means that the information of the fringes is encoded in many small transform coefficients. If the fringe image is noisy, the noise coefficients will have similar magnitude as the fringe coefficients. Directly processing (such as thresholding) the transform coefficients risks removing the fringes together with the noise.

In this paper, a new image enhancement algorithm based on the oriented 2D dual-tree complex wavelet transform (DT-CWT) is proposed for denoising the captured fringe images. The proposed algorithm makes use of the special analytic property of DT-CWT to obtain a sparse representation of the fringe image. We prove that the magnitude response of the oriented 2D DT-CWT coefficients of a fringe image is a piecewise smooth function which can never be achieved by traditional wavelet techniques (such as the 2D discrete wavelet transform (DWT)). Based on the sparse representation, a new iterative regularization procedure is applied for enhancing the noisy fringe image. The new approach introduces an additional preprocessing step to improve the initial guess of the iterative algorithm. The approach is computationally efficient and can suppress noise effectively even when there are sharp phase jumps in the fringe patterns. Compared to the traditional image enhancement techniques, the proposed algorithm achieves a further improvement of 7.2 dB on average in the signal-to-noise ratio (SNR). When applying the proposed algorithm to optical PSP, the new approach enables the reconstruction of 3D models of objects with improved accuracy from 6 to 20 dB in the SNR over the traditional approaches if the fringe images are noisy. Compared to the WFF, the proposed algorithm achieves a similar performance with computational complexity a few orders of magnitude lower.

The organization of this paper is as follows. In Section 2, we first explain why an analytic wavelet transform is a useful tool for analyzing fringe images. We show that by using an analytic wavelet transform, a sparse representation of a fringe image can be obtained. In Section 3, we extend the idea to using a 2D DT-CWT to obtain a sparse representation of fringe images. Then the proposed iterative regularization algorithm based on a 2D DT-CWT is detailed. In Section 4, the simulation and experimental results as compared with the traditional image enhancement methods are presented. In Section 5, a summary of the contributions of this work is given.

2. Fringe Image Analysis Using the Analytic Wavelet Transform

As explained in Section 1, the prerequisite of many image enhancement algorithms is a transform that can give a sparse representation of the image. In this case, the image energy will concentrate on a small number of transform coefficients with large magnitude. It will be much different from the response of noise since for most orthogonal transforms, noise energy will usually spread to many small coefficients in the transform domain. Among the various orthogonal transform techniques, the wavelet transform is a popular choice due to its compactly supported basis functions. Besides, most wavelet functions have high vanishing moments that can annihilate signals of small variation. However, a traditional wavelet transform, e.g., 2D DWT, does not perform normally when applied to fringe images. As mentioned in Section 1, fringe images do not have smooth regions but only fringes, which are indeed sinusoidal functions as given in Eq. (1). Traditional compactly supported wavelet functions, such as the Daubechies wavelet functions, cannot localize the energy of sinusoidal functions due to the aliasing and other problems of the wavelet function. It gives rise to many wavelet coefficients of small magnitude in different scales. To illustrate this, an experiment is done to apply the 2D DWT on the fringe image of the object as shown in Fig. 3(a) with Gaussian noise added. The result is displayed in Fig. 4, where the level 2 wavelet coefficients of the fringe image are shown. We can see that the wavelet coefficients appear in the form of fringes plus noise similar to the original image. Obviously, processing them further (such as thresholding) will be difficult since the fringelike wavelet coefficients are neither sparse nor smooth.

Assume that we have an analytic complex wavelet transform (CWT) such that its wavelet function is analytic (i.e., having zero negative frequency components) and has compact support. The result when applying such analytic CWT to fringe images will be quite different. Let us first consider applying the 1D analytic CWT to each row of a fringe image. Mathematically, it can be written as

$$W_\psi g'_y(a,b) = \int_{-\infty}^{\infty} c(x,y)\cos[w_0 x + \phi(x,y)]\psi\left(\frac{b-x}{a}\right)\left(\frac{1}{a}\right)\mathrm{d}x \qquad (2)$$

for all y. Here, $w_0 = 2\pi f_o$, where f_o is the fundamental frequency of the sinusoidal fringe pattern in the x direction, which has been defined in Eq. (1). We denote g' as the fringe image obtained using the π-shifted PSP procedure as mentioned in Section 1 and ψ as the analytic wavelet function. In Eq. (2), the analytic CWT is applied to a row of fringe image, which can be modeled as a cosine function with a phase shift as described in Eq. (1). Since we assume the support of ψ is small, $c(x,y)$ can be assumed to be constant within the support of ψ. Hence, Eq. (2) can be written as

$$W_\psi g'_y(a,b) = c_y(a,b)\int_{-\infty}^{\infty}\cos[w_0 x + \phi(x,y)]\psi\left(\frac{b-x}{a}\right)\left(\frac{1}{a}\right)\mathrm{d}x. \qquad (3)$$

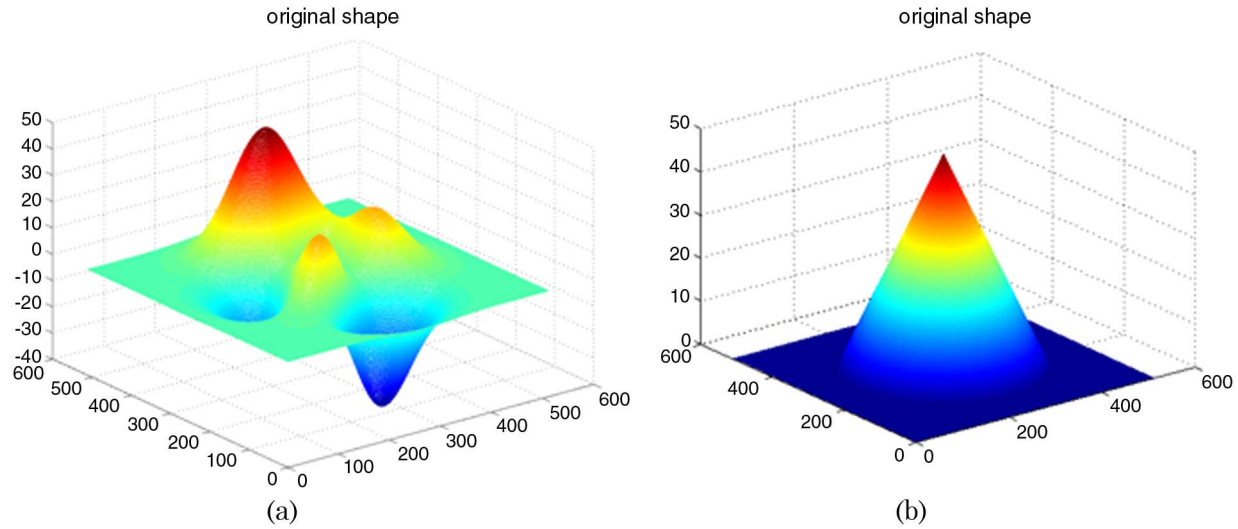

Fig. 3. (Color online) 3D plot of the original shapes used in the simulations: (a) Peaks and (b) Awl.

Assuming the target object has a smooth height profile, $\phi(x,y)$ can also be assumed to be constant within the support of ψ (we shall discuss later the special cases that this assumption is not valid). Then Eq. (3) can be written as

$$W_\psi g'(a,b) = \frac{c(a,b)}{2}\int_{-\infty}^{\infty} e^{-j\frac{w\phi(a,b)}{w_0}} e^{jwb}[\delta(w-w_0) + \delta(w+w_0)]\hat{\psi}(aw)\mathrm{d}w, \quad (4)$$

where $\hat{\psi}$ is the FT of ψ. To simplify the presentation, the parameter y is omitted in the formulation. Since we assume ψ is analytic, all negative frequency components in Eq. (4) become zero. Hence, we have

$$W_\psi g'(a,b) = \frac{c(a,b)}{2}|\hat{\psi}(aw_0)|e^{j(w_0 b-\phi(a,b)+\phi_{\hat{\psi}}(aw_0)} =: B' e^{j\theta}, \quad (5)$$

where $|\hat{\psi}|$ and $\phi_{\hat{\psi}}$ are the magnitude and phase of $\hat{\psi}$, respectively. $|\hat{\psi}(aw_0)|$ is a constant for a given a and w_0. The only variation in B' comes from the term $c(a,b)$, which is normally a very smooth function. Hence, the magnitude response of the wavelet coefficients is actually a very smooth function that can be easily distinguished from noise, if any, in the transform domain. Similar to other denoising applications of the wavelet transform, a simple thresholding can be applied to the magnitude response of the wavelet coefficients and achieves good denoising performance. This result is only possible since the analytic CWT is capable of annihilating negative frequency components for real valued input signals. It cannot be achieved by using the traditional DWT approaches.

In practical situations, it is possible that the target object has abrupt changes in height profile. In this case, the phase changes can be so fast that we cannot approximate $\phi(x,y)$ as constant, although the support of the wavelet kernel is small. Alternatively, we can model such a fringe pattern as the concatenation of fringe patterns with different ϕs, and each of them has a constant value. It is shown in Appendix A that if the wavelet function possesses a vanishing moment larger than 1, the CWT magnitude response will have only small fluctuation at the meeting point of two fringe patterns and it will have a fast decay rate. Therefore, such a CWT magnitude response can be seen as a piecewise smooth signal. To illustrate this effect, a testing object "Awl" as shown in Fig. 3(b) is used as an example. Figure 5(b) shows its fringe pattern, and a slice of it (row 256) is shown in Fig. 6. For the implementation of the analytic CWT, we use the DT-CWT, which is a good approximation of the analytic CWT and with fast implementation algorithms. Figure 7 shows two levels of DT-CWT coefficients. As shown in Fig. 6, the fringe

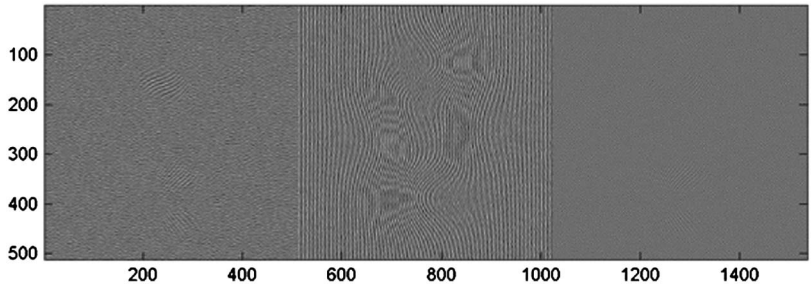

Fig. 4. Undecimated 2D DWT of a noisy fringe image, level 2: H, V, and D subbands.

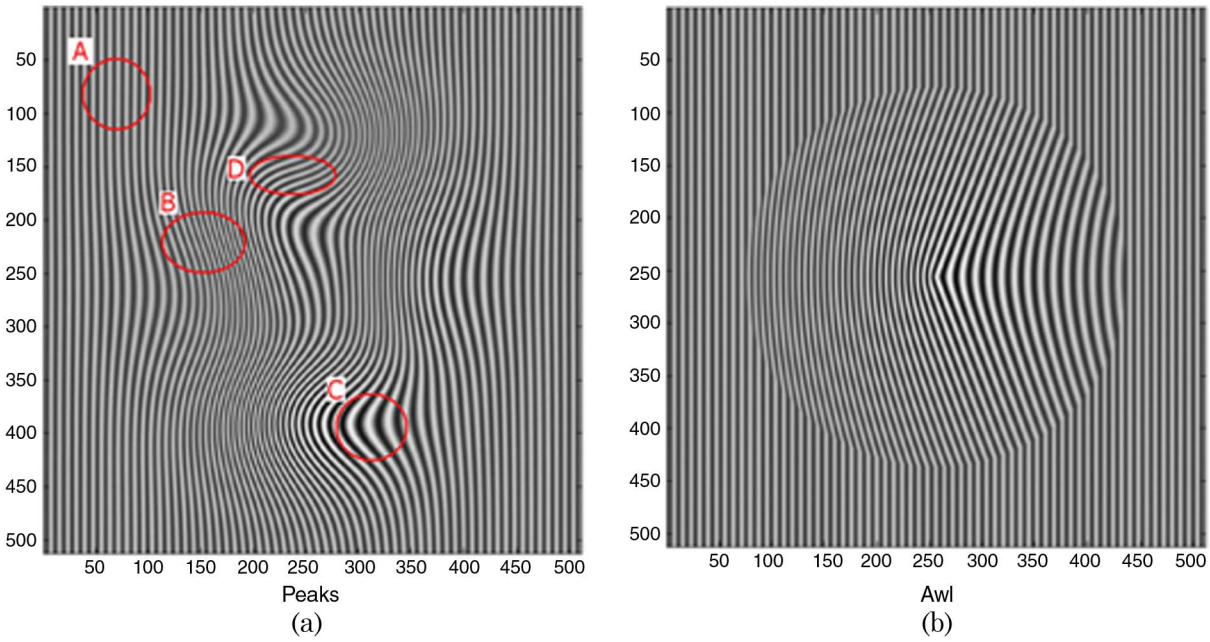

Fig. 5. (Color online) Clean fringe images.

pattern has a sharp phase change at a position around 250. As mentioned above, we model it as the concatenation of two fringe patterns, each of which has a smooth phase change. The envelopes in Fig. 7 are the magnitude response of the DT-CWT coefficients. They are normally smooth functions but with a sudden jump at the concatenation point. The overshoot or undershoot around the sudden jump does not have large magnitude and decays rapidly. Hence, it is safe for us to conclude that the analytic CWT magnitude response can be modeled as a piecewise smooth function. Traditional wavelet denoising techniquea can then be applied if the fringe image is noisy.

3. Proposed Algorithm

Based on the above result, a new algorithm for the enhancement of fringe images is proposed in this section. The new algorithm makes use of the DT-CWT, which is a good approximation of the analytic CWT, as mentioned in Section 2, to obtain a sparse representation of the fringe images. We extend the idea to two dimensions so that we can take into account the orientation of the fringe image, which is a useful feature that facilitates the design of efficient denoising algorithms.

Similar to the 1D case, it can be shown that the magnitude response of the 2D DT-CWT coefficients can also be modeled as a 2D piecewise smooth function. As can be seen in Fig. 5(a) (which is the fringe image of the object in Fig. 3(a)), a fringe image can be divided into different subimages with fringes oriented at different angles (see the differences among regions A, B, C, and D). Each subimage can be modeled as a 2D cosine function as

$$g'(x,y) = c(x,y)\cos[u_0 x + v_0 y + \phi_r(x,y)], \qquad (6)$$

where u_0 and v_0 are the fundamental frequencies (in radians) of the cosine function in the x and y directions, respectively. $\phi_r(x,y)$ is the 2D phase shift. For a small region in a subimage, both $c(x,y)$ and $\phi_r(x,y)$ can be assumed to be constant since the target object usually has a smooth height profile

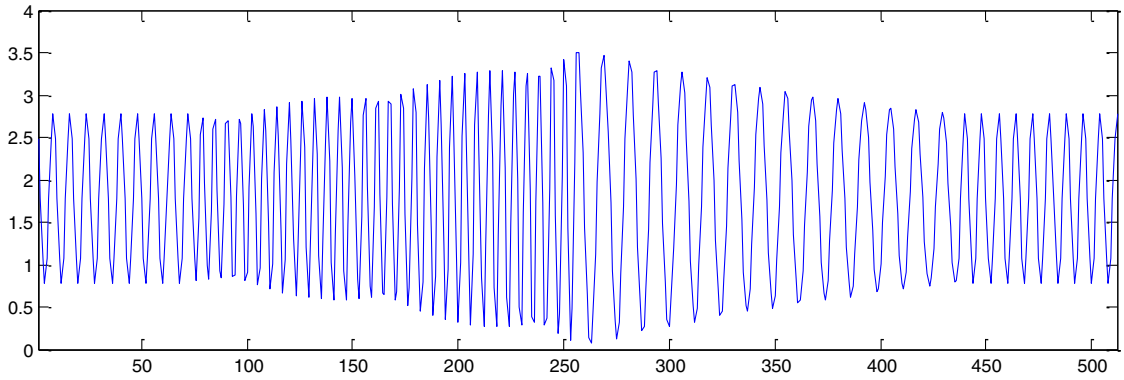

Fig. 6. (Color online) Row 256 for Awl fringe pattern.

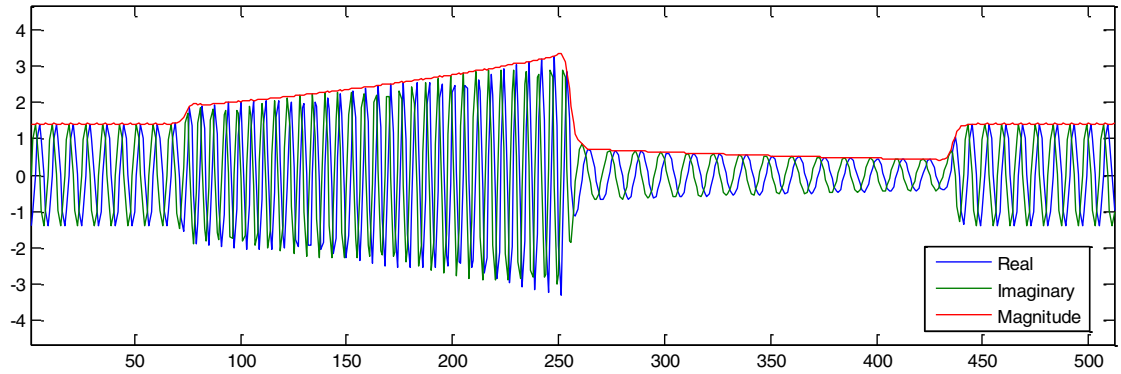

Level 1 DT-CWT coefficients.

(a)

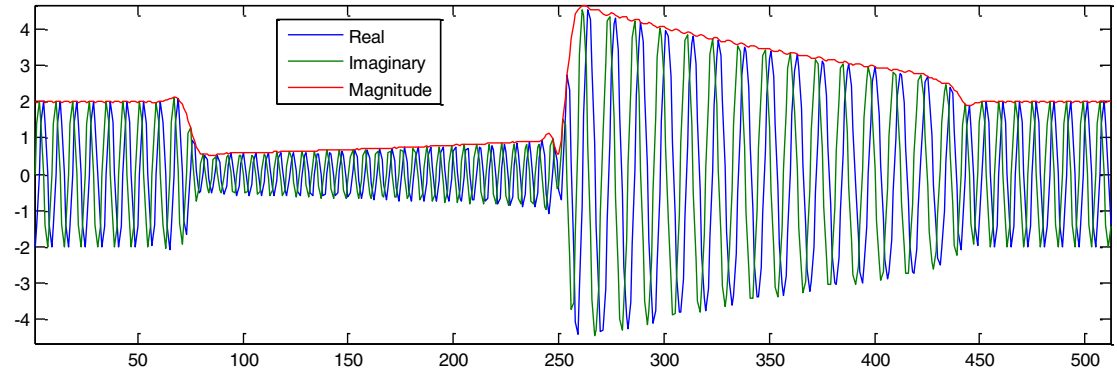

Level 2 DT-CWT coefficients.

(b)

Fig. 7. (Color online) (a) Level 1 and (b) level 2 DT-CWT coefficients for row 256 of the Awl fringe pattern.

(for the case that the target object has abrupt changes in its height profile, we can always consider it as the concatenation of subimages as mentioned in Section 2). In the frequency domain, $g'(x,y)$ can be written as

$$\hat{g}'(u,v) = \frac{c}{2} e^{j\phi_r u/u_0}[\delta(u-u_0)\delta(v-v_0) + \delta(u+u_0)\delta(v+v_0)]. \tag{7}$$

It means that $\hat{g}(u,v)$ contains a pair of delta functions at mirror positions of the 2D Fourier spectrum with a point of reflection at the origin. Therefore, the transformation of $g'(x,y)$ using the 2D analytic CWT is given by

$$\begin{aligned} W_\psi g'(a,b_x,b_y) &= \int_{-\infty}^{\infty}\int_{-\infty}^{\infty} c(x,y)\cos[u_0 x + v_0 y + \phi_r(x,y)]\psi\left(\frac{b_x-x}{a},\frac{b_y-y}{a}\right)\left(\frac{1}{a^2}\right)\mathrm{d}x\mathrm{d}y \\ &= \int_{-\infty}^{\infty}\int_{-\infty}^{\infty}\frac{c(a,b_x,b_y)}{2} e^{j\phi_r(a,b_x,b_y)u/u_0}[\delta(u-u_0)\delta(v-v_0)+\delta(u+u_0)\delta(v+v_0)]\cdot\hat{\psi}(au,av)e^{jub_x}e^{jvb_y}\mathrm{d}u\mathrm{d}v \\ &= \frac{c(a,b_x,b_y)}{2} e^{j(u_0 b_x+v_0 b_y+\phi_r(a,b_x,b_y)}\hat{\psi}(au_0,av_0) = \frac{c(a,b_x,b_y)}{2}|\hat{\psi}(au_0,bv_0)|e^{j(u_0 b_x+v_0 b_y-\phi_r(a,b_x,b_y)+\phi_{\hat{\psi}}(au_0,bv_0)} \\ &=: B' e^{j\theta}, \end{aligned} \tag{8}$$

where ψ is the wavelet function and we have made use of the analytic property of the function. Eq. (8) shows that the magnitude response of the 2D wavelet coefficients is a 2D smooth function similar to that in Eq. (5). As the target object can have abrupt changes in its height profile, the magnitude response of the whole image can be considered as a 2D piecewise smooth function.

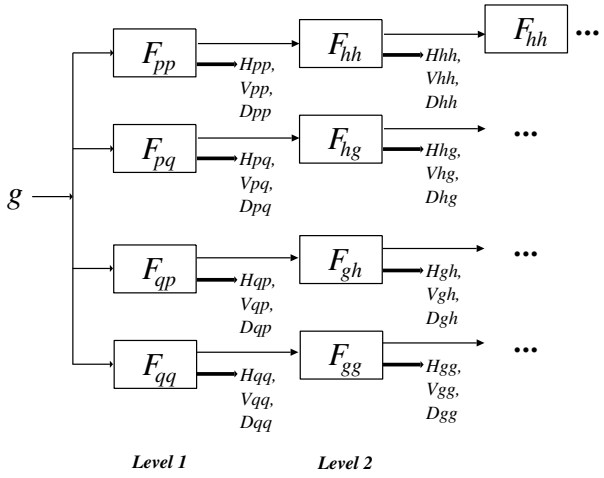

Fig. 8. Oriented 2D DT-CWT (two levels are shown).

As mentioned above, the oriented 2D DT-CWT [25] is a good approximation of the 2D analytic CWT and with fast algorithms for its implementation. It is adopted in the proposed algorithm. The oriented 2D DT-CWT is realized using four separate DWT trees as shown in Fig. 8. As indicated in [25], the filters used for the first stage are different from the rest. For implementation, we adopt the wavelet filters as described in the example of [26]. At each level, there are four sets (due to four trees) of subband data. For each subband, it can further be divided into $\{H,V,D\}$, which represent the horizontally, vertically and diagonally oriented wavelet coefficients, respectively. For example, at level 1, the wavelet coefficients generated by the four trees are $\{H_{pp},V_{pp},D_{pp}\}$, $\{H_{pq},V_{pq},D_{pq}\}$, $\{H_{qp},V_{qp},D_{qp}\}$, and $\{H_{qq},V_{qq},D_{qq}\}$, as can be seen in Fig. 8. Six oriented complex subbands, namely R_{H1}, R_{V1}, R_{D1}, R_{H2}, R_{V2}, and R_{D2} can be constructed as follows (for simplicity, only the first level is shown):

$$R_{H1} = (Hpp - Hqq) + j(Hqp + Hpq); \quad (9)$$

$$R_{V1} = (Vpp - Vqq) + j(Vqp + Vpq); \quad (10)$$

$$R_{D1} = (Dpp - Dqq) + j(Dqp + Dpq); \quad (11)$$

$$R_{H2} = (Hpp + Hqq) + j(Hqp - Hpq); \quad (12)$$

$$R_{V2} = (Vpp + Vqq) + j(Vqp - Vpq); \quad (13)$$

$$R_{D2} = (Dpp + Dqq) + j(Dqp - Dpq). \quad (14)$$

To simplify the notations, let us denote $\bar{R}_1 = \{R_{H1},R_{V1},R_{D1}\}$ and $\bar{R}_2 = \{R_{H2},R_{V2},R_{D2}\}$. An example of the oriented 2D DT-CWT of a clean fringe image is shown in Fig. 9. In the figure, the magnitude response of the six subbands $\{\bar{R}_1,\bar{R}_2\}$ is shown. It can be seen that they no longer exist in the form of fringes; rather, they look like smooth images with edges. It is very different from that generated by a traditional 2D DWT as shown in Fig. 4. It verifies our discussion above.

Knowing that $\{\bar{R}_1,\bar{R}_2\}$ are in the form of a 2D piecewise smooth function, a denoising algorithm can be readily designed. The noise contamination process of fringe images can be modeled with the following formulation:

$$y = g' + n = W^+ g_w + W^+ n_w, \quad (15)$$

where W^+ is the inverse-oriented 2D DT-CWT, y and g' are the observed noisy fringe image and the original clean fringe image, respectively, $n \sim N(0,\sigma^2)$ is the additive noise, and g_w and n_w are the wavelet coefficients of g' and n, respectively. Here we have used the linear property of the oriented 2D DT-CWT. Following the idea in [20–24], the denoising of fringe images can be formulated as the following optimization problem:

$$\arg\min_{g_w} \frac{1}{2}\|W^+ g_w - y\|^2 + \lambda \cdot \rho(g_w), \quad (16)$$

where ρ is a convex function and, in our case, we select $\rho = |g_w|$. To obtain a good estimation of g_w, an iterative procedure was suggested in [20–24] as

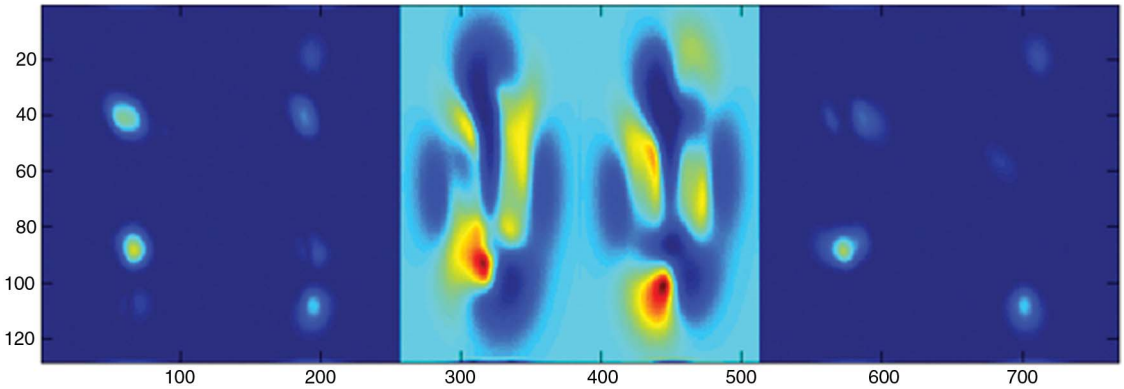

Fig. 9. (Color online) Oriented 2D DT-CWT magnitude response of clean fringe image, level 2 of the R_{H1}, R_{H2}, R_{V1}, R_{V2}, R_{D1}, and R_{D2} subbands (from left to right, respectively).

$$g_w^{k+1} = \eta(W(y - W^+ g_w^k) + g_w^k, \lambda)), \quad (17)$$

where g_w^k is the estimation of g_w at the kth iteration. η is the shrinkage function for complex numbers defined as

$$\eta(x, \lambda) = \max(0, |x| - \lambda) \exp(j.\angle x), \quad (18)$$

where $\angle x$ refers to the phase angle of x. λ is the threshold used in the shrinkage function. The universal threshold [27] is adopted in the proposed algorithm since the noise distribution is approximately additive white Gaussian noise.

Although the above algorithm gives a good performance in terms of SNR, it needs to be further refined in order to apply to real time profilometry applications. As it is different from general image denoising, the residue noise remaining in the enhanced fringe images can be detrimental to the subsequent phase unwrapping process since error can propagate and introduce great visual distortion to the reconstructed 3D model. In general, the residue noise level can be lowered by reducing the step size and increasing the number of iterations of the optimization. It, however, can increase the computation time such that the resulting algorithm will not be suitable for real time applications. Alternatively, a good initial guess can help to improve the optimization without increasing the number of iterations. For this reason, we introduce an additional preprocessing step by using a median filter to generate the initial estimate for the iterative process. More specifically, let

$$g_w^0 = med(|\eta(Wg', \lambda))|, N_x, N_y). \exp(j.\angle Wg'), \quad (19)$$

where *med* is a 2D median filter with a rectangular window of size $N_x \times N_y$. The size of the median filters for subband $\{H, V, D\}$ of $\{\bar{R}_1, \bar{R}_2\}$ is selected to be 3×5, 5×3 and 5×5 (row $\times$ column), respectively. It is based on the observation that there is much correlation between vertical (or horizontal) neighboring coefficients for subband V (or H). Then let

$$\hat{y} = W^+(g_w^0). \quad (20)$$

Eq. (17) is modified as

$$g_w^{k+1} = \eta(W(\hat{y} - W^+ g_w^k) + g_w^k, \lambda)). \quad (21)$$

Compared with g_w, g_w^0 contains much less large-magnitude outliers due to the median filtering operation. Such outliers are presumably caused by noise since, as can be seen in Fig. 9, the magnitude response of fringe images should be a piecewise smooth function. Eq. (20) provides a good initial guess of y that facilitates fast convergence of the iterative process in Eq. (21). In general, a very good result can be achieved by iterating Eq. (21) four to five times. We would like to stress that the reason the simple median filter can be effectively applied to generate the initial estimate is that the oriented 2D DT-CWT of fringe images is a piecewise smooth function. The same performance can hardly be achieved if applying the median filter to the original fringe images or the wavelet coefficients generated by using a 2D DWT. Besides, we have adopted the orientation of different subbands in the design of the median filters. They all benefit from the special properties of the oriented 2D DT-CWT when applied to fringe images.

The proposed fringe image enhancement algorithm is summarized below.

Algorithm-Oriented 2D DT-CWT Iterative Shrinkage Fringe Image Enhancer (DTISE)

For a fringe image captured based on PSP, $g'(x, y)$,

1. Compute L levels of oriented 2D DT-CWT on $g'(x, y)$, i.e., $Wg' := \{A^L(u, v), g_w := \bar{R}_k^r(u, v)\}$; $r = 1, ..., L; k = 1, 2\}\}$.
2. Set the scaling coefficients to zero: $\hat{A}^L(u, v) = 0$.
3. Generate the initial estimate g_w^0 based on Eq. (19).
4. Apply g_w^0 to Eqs. (20) and (21) and iterate N times.

$\hat{A}^L(u, v)$ is the coarsest scaling coefficient which should be set to zero since there should not be dc components in a fringe image. As mentioned above, good enhancement results can be achieved with a very small number of iterations, such as 5. The enhanced image is then further processed with a phase unwrapping technique in order to estimate the phase and then reconstruct the 3D model of the target object. As we will show in Section 4, the proposed algorithm greatly improves the robustness of the phase unwrapping process when working with noisy fringe images.

4. Evaluations

A. Computational Complexity

An analysis is made in Appendix B to evaluate the computational complexity of the proposed algorithm DTISE and compare it with the recently proposed WFF technique [15–19] as mentioned in Section 1. In Table 1, the approximate number of floating point operations of the proposed algorithm and WFF for various fringe image sizes and parameters are listed. In the table, N_w refers to the number of vertical and horizontal frequency points for WFF. As mentioned in Section 3, the proposed algorithm DTISE adopts the oriented 2D DT-CWT implemented by using four 2D DWT trees applied to all rows and then columns of a fringe image separately. For each 2D DWT tree, the length of the wavelet filters is set to 12, which is typical for wavelet filters. The table clearly shows that the number of operations required for the proposed algorithm is far less than that of WFF, at a ratio from 1 : 27 to 1 : 259.

To evaluate the real processing speed of the proposed algorithm DTISE and WFF, we realize them with MATLAB running on a general personal

Table 1. Approximate Number of Floating Point Operations (Flops) of the Proposed DTISE (Five Iterations) and WFF for Various Fringe Image Sizes and Parameters

	N_w	64×64	128×128	256×256	512×512	1024×1024
C_{WFF}	17	2.48×10^9	1.14×10^{10}	5.19×10^{10}	2.32×10^{11}	1.02×10^{12}
	21	3.79×10^9	1.74×10^{10}	7.92×10^{10}	3.54×10^{11}	1.56×10^{12}
	27	6.27×10^9	2.89×10^{10}	13.09×10^{10}	5.85×10^{11}	2.58×10^{12}
	41	14.46×10^9	6.66×10^{10}	30.19×10^{10}	13.48×10^{11}	5.96×10^{12}
C_{DTISE}	-	8.9×10^7	3.6×10^8	1.4×10^9	5.7×10^9	2.3×10^{10}

computer. For WFF, we used the code (wft2f.m) released by the authors of [15–19]. In the simulation, we used 3D model "peaks" derived from the MATLAB function "peaks" of size 512 pixels × 512 pixels and scaled by 6 (for much steeper slopes) as shown in Fig. 3(a). We then computed the fringe images g' of this 3D model as shown in Fig. 5(a) using the π-shifted PSP approach. The fringe images were then added with independent and identically distributed white Gaussian noise (with standard deviation $\sigma = 1.5$). Table 2 shows the processing times and performance in terms of SNR when different N_ws are used. Concurring with the analysis on computational complexity, the processing time required by the proposed algorithm is much less than by WFF for all N_ws. For example, the processing time required by the proposed algorithm is only 1/16 of the WFF when $N_w = 17$ with a gain of 1.5 dB in SNR. This reduction in computational complexity enables the proposed algorithm to be more suitable for real time applications.

B. Performance in Simulations and Experiments

In this section, we first show the performance of different algorithms when enhancing noisy fringe images. For a fair comparison, we selected another recently proposed nonlinear filtering approach [2] that can also be used in real time applications. We dub such method as M-NLF. We also compared the proposed DTISE algorithms with the traditional wavelet shrinkage denoising method using 2D DWT to illustrate the improvement of 2D DT-CWT over 2D DWT in fringe image denoising. In this simulation, the testing object "Awl" as shown in Fig. 3(b) was used. We first computed the fringe image of the testing object, then white Gaussian noise at different noise levels was added. For the proposed DTISE and wavelet shrinkage algorithms, the traditional universal threshold was used to denoise the images. Figure 10 shows the comparison result. It can be seen that the proposed DTISE-1 algorithm outperforms the other two traditional approaches with an average improvement of 7.2 dB in SNR. Since DTISE-1 is different from the wavelet shrinkage mainly in the transform used to obtain the sparse representation of the fringe images, the improvement of 2D DT-CWT over 2D DWT can easily be seen. A sample of the enhanced image given by different algorithms is shown in Fig. 11. The proposed DTISE-5 gives the best result, although it has a slightly higher computational complexity than DTISE-1.

Next, we evaluated the quality of the reconstructed 3D model based on the enhanced fringe images using different enhancement algorithms. For this comparison, another more challenging 3D model "Peaks" as shown in Fig. 3(a) was used. Using the enhanced fringe images, reconstruction of the 3D model was performed with Goldstein's phase unwrapping method [9]. In Fig. 12, the reconstructed 3D models based on the fringe images enhanced by using M-NLF [2] and the proposed DTISE (one and five iterations) are shown. The SNRs with respect to the true model are respectively 9.39, 32.20 (one iteration), and 35.70 dB (five iterations). It can be seen in Fig. 12 that using only Goldstein's phase unwrapping method cannot avoid having a severe error in the reconstructed 3D model at this noise level. Using a fringe image enhancer can significantly improve the robustness of the phase unwrapping process, although the improvement of M-NLF [2] is incomparable to the proposed DTISE. Figure 13 further illustrates the quality of the reconstructed 3D model in terms of SNR when using different enhancement methods at different noise levels. It shows that the difference in SNR of using M-NLF

Table 2. Execution Time for Enhancing a 512 × 512 "Peaks" Fringe Image

	N_w	Time (seconds)	SNR (decibels)
WFF	14	61.588	33.8
	17	89.601	34.3
	21	136.685	39.9
	27	225.907	42.9
	41	522.316	43.28
DTISE (five iterations)	-	5.455	35.70

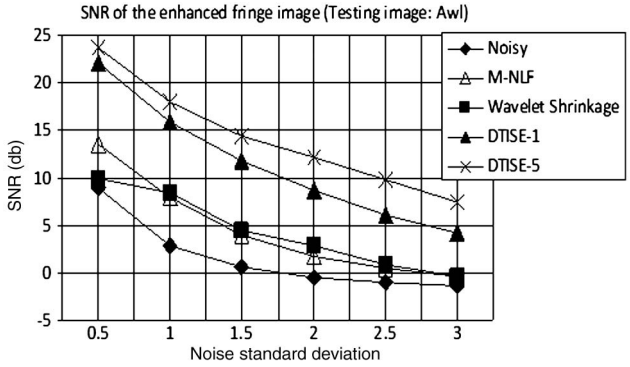

Fig. 10. SNR of the enhanced fringe image using different enhancement approaches.

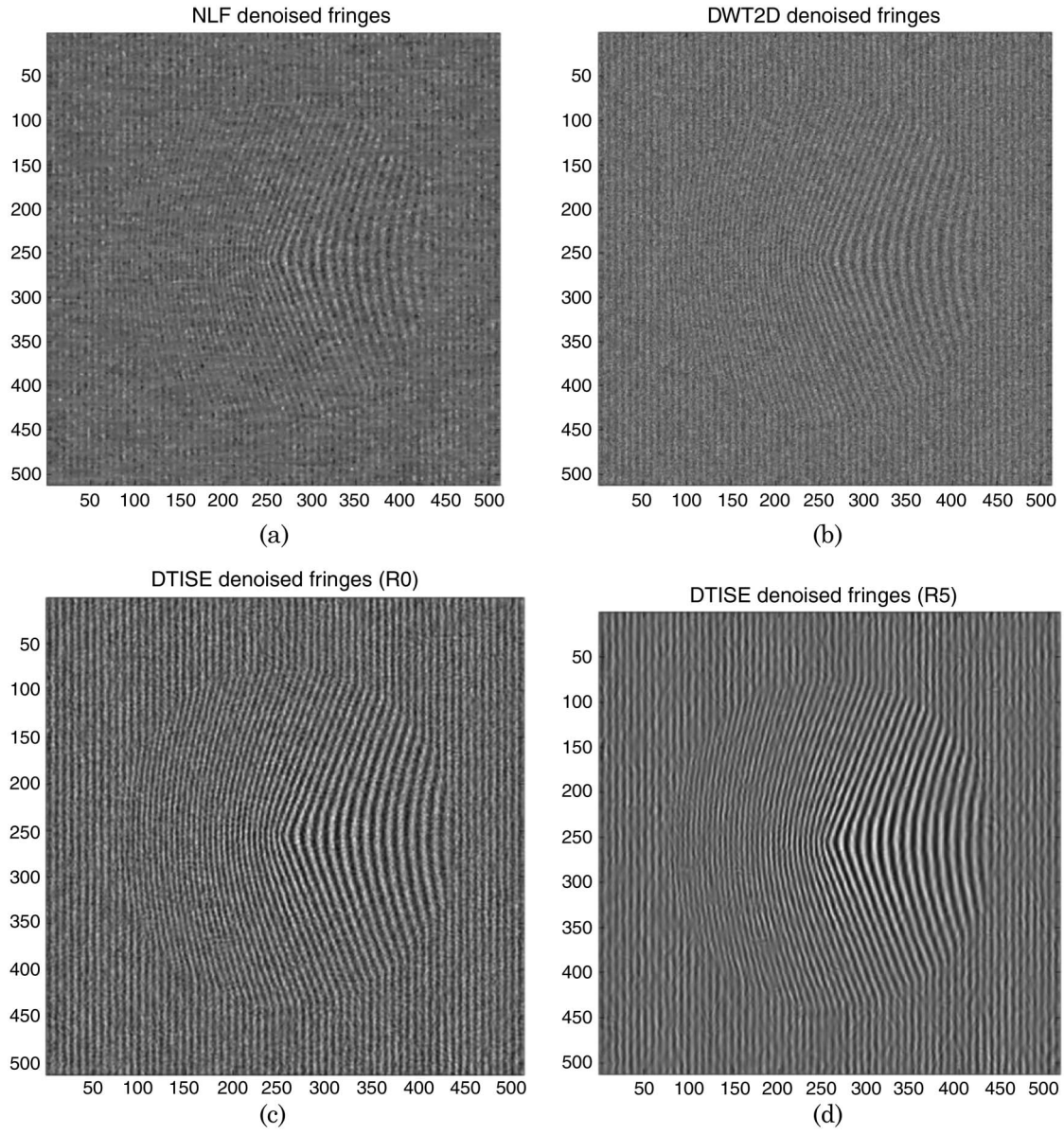

Fig. 11. Enhanced fringe images using different algorithms, noise $\sigma = 2.5$ (a) M-NLF, (b) wavelet shrinkage, (c) DTISE-1, (d) DTISE-5.

[2] and the proposed DTISE can be even bigger when the noise level is higher.

We further tested the proposed algorithms in a reconstruction experiment with a real object. We used a paper cone as the testing 3D object as shown in Fig. 2. The fringe images were captured using a digital single-lens reflex (SLR) camera with a 50 mm lens at aperture $f/16$. Two settings were selected in the experiment: (1) ISO100, 1/10 s exposure; and (2) ISO1600, 1/320 s. The purpose of setting (2) is to create an extreme environment so as to illustrate the improvement of the proposed algorithms to the phase unwrapping process. For setting (1), the captured fringe image and the reconstructed 3D model using π-shifted PSP with Goldstein's phase unwrapping algorithm [9] are shown in Figs. 14(a) and 15(a), respectively. For setting (2), the same are shown in Figs. 14(b) and 15(b). It can be seen that the noisy fringe image greatly affects the reconstruction quality even using a powerful phase unwrapping algorithm. In Figs. 14(c) and 14(d), the enhanced fringe images using the proposed DTISE and M-NLF [2] are shown. The corresponding reconstruction results are shown in Figs. 15(c) and 15(d). For the proposed algorithm, the quality of the reconstruction is just as good as when using a much longer exposure time and a smaller ISO, as shown in Fig. 15(a). However, it cannot be achieved with the traditional M-NLF approach [2].

5. Summary

In this paper, we investigated the enhancement method of fringe images based on the oriented 2D DT-CWT. We first showed that enhancing the fringe images is important to real time profilometry applications since even with using state-of-the-art phase

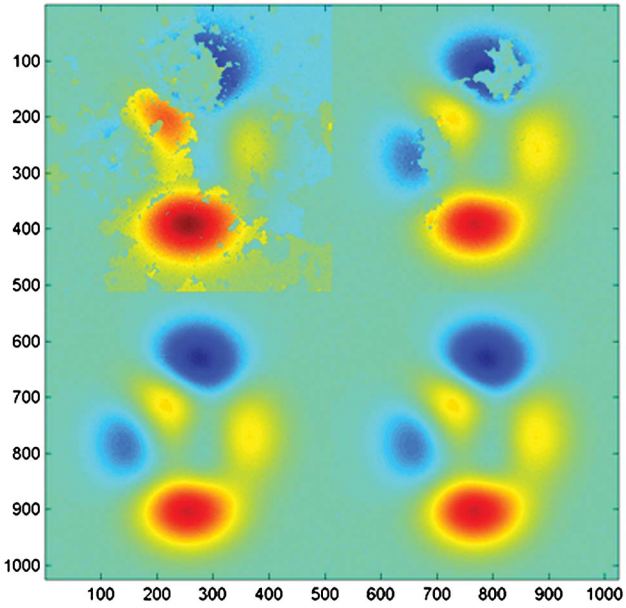

Fig. 12. (Color online) Reconstruction using Goldstein's phase unwrapping method from noisy fringe images (top left), enhanced fringe images using M-NLF (median filter plus nonlinear filtering approach) [2] (top right), and proposed DTISE: initial estimate (bottom left) and after five iterations (bottom right) for noise $\sigma = 1.5$.

unwrapping methods, it still may not be possible to avoid having severe distortion in the reconstructed 3D model if the captured fringe images are noisy. We then showed that, as opposed to the traditional wavelet transform, the oriented 2-D DT-CWT effectively gives a sparse representation of fringe images because oriented 2-D DT-CWT of fringe images give a piecewise smooth magnitude response. Based on this finding, we proposed an iterative fringe image denoising algorithm, namely DTISE. It is different from the traditional wavelet-based iterative regularization methods in that a preprocessing step is introduced that gives a better initial estimate. The proposed preprocessing step significantly reduces the outliers in the enhanced images, which is important to the subsequent phase unwrapping process. The proposed DTISE algorithm is effective yet efficient. As compared to traditional real time enhancement methods such as the nonlinear filtering in [2], the proposed algorithm gives a much lower level of reconstruction error. As compared to the WFF enhancement method which delivers the best performance (as far as we know), the proposed DTISE algorithms give competitive performance but have a much lower computational complexity, which facilitates real time optical profilometry applications.

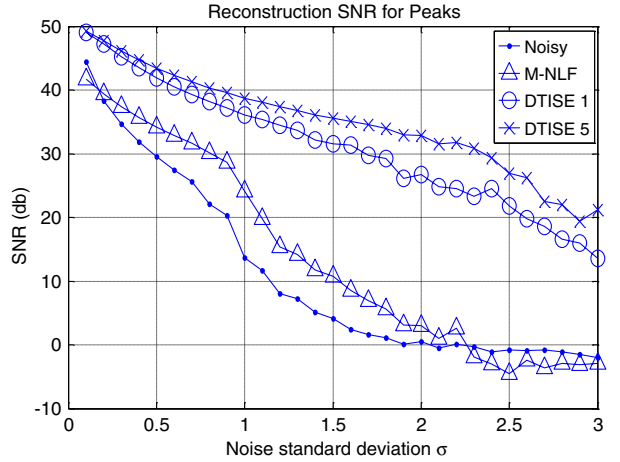

Fig. 13. (Color online) Average reconstruction SNR using different enhancement approaches.

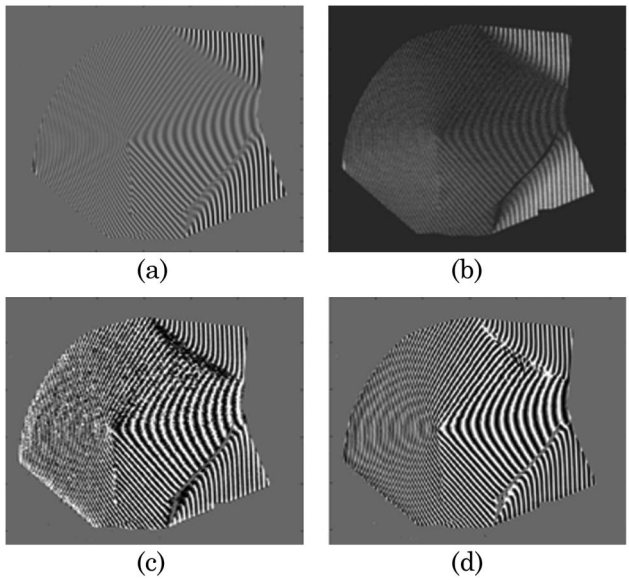

Fig. 14. Fringe images captured at (a) ISO100, exposure 1/10 s; (b) ISO1600, exposure 1/320 s; (c) result of using M-NLF [2] on (b); and (d) result of using the proposed DTISE (five iterations) on (b).

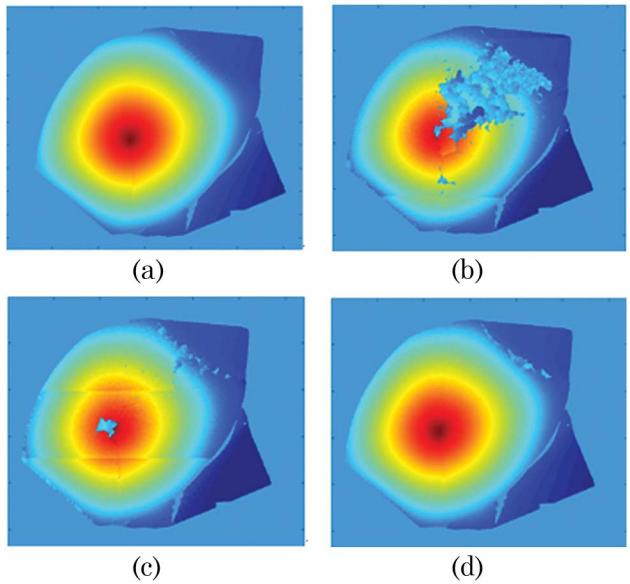

Fig. 15. (Color online) Reconstructed 3D model using Goldstein's phase unwrapping method from fringe images captured at (a) ISO100, exposure 1/10 s; (b) ISO1600, exposure 1/320 s; (c) result of using M-NLF [2] on (b); and (d) result of using the proposed DTISE (five iterations) on (b).

Appendix A: Analytic CWT Response for Concatenated Fringe Patterns

Without loss of generality, let us consider the case that a concatenation of fringe patterns happens at the origin. It reads

$$f(x) = B\cos(w_0 x + \phi)u(x) = g(x)u(x), \tag{A1}$$

where $u(x)$ denotes the Heaviside step function, with the FT $F\{u\}(w) = \pi\left[\frac{1}{(j\pi w)+\delta(w)}\right]$. Then the FT of Eq. (A1) is

$$\begin{aligned} F\{f\}(w) &= \int_{-\infty}^{\infty} F\{u\}(y)F\{g\}(w-y)\mathrm{d}y \\ &= \frac{B}{2}\left\{e^{-j\phi}\left[\delta(w-w_0) + \frac{1}{j\pi(w-w_0)}\right]\right. \\ &\quad \left. + e^{j\phi}\left[\delta(w+w_0) + \frac{1}{j\pi(w+w_0)}\right]\right\}. \end{aligned} \tag{A2}$$

The analytic CWT of f can be written as

$$\begin{aligned} W_{\psi_A}\{f\}(a,b) &= \int_{-\infty}^{\infty} F\{f\}(w)e^{jbw}\hat{\psi}(aw)\mathrm{d}w \\ &= B'|\hat{\psi}_A(aw_0)|e^{j[w_0 b-\phi+\phi_\psi(aw_0)]} \\ &\quad + \frac{B}{2}\int_{-\infty}^{\infty}\frac{1}{j\pi}\left(\frac{e^{-j\phi}}{w-w_0}\right. \\ &\quad \left. + \frac{e^{j\phi}}{w+w_0}\right)e^{jwb}\hat{\psi}(aw)\mathrm{d}w. \end{aligned} \tag{A3}$$

The first part of Eq. (A3) is the same as Eq. (5). Some simple calculation on the second term of Eq. (A3) yields

$$\begin{aligned} &\frac{B}{2j\pi}\int_{-\infty}^{\infty}\frac{1}{w}e^{jwb}\{e^{-j\phi+jw_0 b}\hat{\psi}_A[a(w+w_0)] \\ &\quad + e^{j\phi-jw_0 b}\hat{\psi}_A[a(w-w_0)]\}\mathrm{d}w. \end{aligned} \tag{A4}$$

From Theorem 6.2 of [28], a wavelet with fast decay has n vanishing moments if and only if there exists ψ_2 with a fast decay such that $\hat{\psi}(w) = (-jw)^k\hat{\psi}_2(w)$ for $k = 0,\ldots,n-1$. We may rewrite Eq. (A4) as

$$\begin{aligned} &\frac{-B}{2\pi}\int_{-\infty}^{\infty}e^{jwb}\{e^{-j\phi+jw_0 b}\hat{\psi}_{A2}[a(w+w_0)] \\ &\quad + e^{j\phi-jw_0 b}\hat{\psi}_{A2}[a(w-w_0)]\}\mathrm{d}w, \end{aligned} \tag{A5}$$

which gives bounded perturbation on the first term of Eq. (A3).

Appendix B: Computational Complexity

The proposed algorithm adopts the oriented 2D DT-CWT which consists of four independent 2D DWT decompositions. For a fringe image with size $N \times M$, the complexity for performing the oriented 2D DT-CWT and its inverse is given by

$$\begin{aligned} &C_{\mathrm{ODT2D-CWT}}(N,M,L) \\ &\approx 4C_{\mathrm{DWT}}(N,M,L) + NM\left(1-\frac{1}{2^{2L}}\right)C_{\mathrm{subband}} \\ &\approx 4C_{\mathrm{DWT}}(N,M,L) + NMC_{\mathrm{subband}}, \end{aligned} \tag{B1}$$

where C_{subband} denotes the operations required to compute the magnitude and phase of the complex wavelet coefficients $\bar{R}_1$ and $\bar{R}_2$ from the four 2D DWT trees, $C_{\mathrm{subband}} = 4C_{\mathrm{add}} + (2C_{\mathrm{add}} + 2C_{\mathrm{sqrt}} + 4C_{\mathrm{sq}} + 2C_{\mathrm{atan2}})$. The complexity of direct DWT realization is

$$\begin{aligned} C_{\mathrm{DWT}}(N,M,L) &\approx \frac{1-4^{-L}}{1-4^{-1}}NM(N_f C_{\mathrm{mult}} + (N_f-1)C_{\mathrm{add}}) \\ &\approx \frac{4}{3}NM(N_f C_{\mathrm{mult}} + (N_f-1)C_{\mathrm{add}}), \end{aligned} \tag{B2}$$

where N_f denotes the filter length. The inverse 2D DWT takes the same complexity as the forward transform. Therefore, the complexity of the inverse oriented 2D DT-CWT is

$$\begin{aligned} C_{\mathrm{IODT2D-CWT}}(N,M,L) &\approx 4C_{\mathrm{IDWT}}(N,M,L) \\ &\quad + NMC_{\mathrm{Isubband}}, \end{aligned} \tag{B3}$$

where $C_{\mathrm{Isubband}} = (4C_{\mathrm{mult}} + 2C_{\mathrm{sin}} + 2C_{\mathrm{cos}}) + 4C_{\mathrm{add}}$. Computing the initial estimate g_w^0 requires shrinkage followed by median filtering on the transform coefficient magnitudes. The complexity is given by

$$\begin{aligned} C_{dn0}(N,M,L) &\approx 2NM\left(1-\frac{1}{2^{2L}}\right)\left(C_{\mathrm{shrink}}\right. \\ &\quad \left. + C_{\mathrm{median\ Filter}}\right). \end{aligned} \tag{B4}$$

Each iteration requires subtraction of $\hat{y}$ and $W^+ g_w^k$ in Eq. (21), the addition of the resulting coefficients and the shrinkage operation. Hence, the complexity for these operations becomes

$$\begin{aligned} C_{dn1}(N,M,L) &\approx 2NM\left(1-\frac{1}{2^{2L}}\right)C_{\mathrm{shrink}} \\ &\quad + 4NM\left(1-\frac{1}{2^{2L}}\right)C_{\mathrm{add}} + \mathrm{NMC_{add}}. \end{aligned} \tag{B5}$$

Therefore, the complexity for the generation of the initial estimate becomes

$$
\begin{aligned}
C_{\mathrm{DTISE0}} &= C_{\mathrm{ODT2D-CWT}}(N,M,L) \\
&\quad + C_{\mathrm{IODT2D-CWT}}(N,M,L) + C_{dn0}(N,M,L) \\
&\approx \mathrm{NMC}_{\mathrm{add}}\left(\frac{32}{3}\left(N_f-1\right)+11\right) \\
&\quad + NMC_{\mathrm{mult}}\left(\frac{32}{3}N_f+8\right) \\
&\quad + 2NM(C_{\sin}+C_{\cos}+C_{\mathrm{atan2}} \\
&\quad + C_{\mathrm{sqrt}}+C_{\mathrm{median\ Filer}}).
\end{aligned} \tag{B6}
$$

And the complexity of each iteration becomes

$$
\begin{aligned}
C_{\mathrm{DTISE1}} &= C_{\mathrm{ODT2D-CWT}}(N,M,L) \\
&\quad + C_{\mathrm{IODT2D-CWT}}(N,M,L) + C_{dn1}(N,M,L) \\
&\approx NMC_{\mathrm{add}}\left(\frac{32}{3}\left(N_f-1\right)+16\right) \\
&\quad + \mathrm{NMC}_{\mathrm{mult}}\left(\frac{32}{3}N_f+8\right) + 2NM(C_{\sin}+C_{\cos} \\
&\quad + C_{\mathrm{atan2}}+C_{\mathrm{sqrt}}).
\end{aligned} \tag{B7}
$$

Current computing technology enables similar execution time for addition and multiplication (C_{op}), i.e., $C_{\mathrm{mult}} \approx C_{\mathrm{add}}$ and $C_{\mathrm{shrink}} \approx C_{\mathrm{add}}$; sine, cosine, atan2 and square root approximately require 5, 5, 10, and $20\,C_{\mathrm{op}}$, respectively; and a 5×5 median filter requires around $50\,C_{\mathrm{op}}$. Without further optimization on memory input/output, the complexity of the proposed algorithm can be approximated as

$$
\begin{aligned}
C_{\mathrm{DTISE0}} &\approx \mathrm{NMC}_{\mathrm{op}}\left(\frac{32}{3}\left(N_f-1\right)+11+\frac{32}{3}N_f+8\right. \\
&\quad \left.+2(5+5+10+20+50)\right) \\
&= \mathrm{NMC}_{\mathrm{op}}\left(\frac{64}{3}N_f-\frac{32}{3}+199\right),
\end{aligned} \tag{B8}
$$

$$
\begin{aligned}
C_{\mathrm{DTISE1}} &\approx \mathrm{NMC}_{\mathrm{op}}\left(\frac{32}{3}\left(N_f-1\right)+16+\frac{32}{3}N_f\right. \\
&\quad \left.+8+2(5+5+10+20)\right) \\
&= \mathrm{NMC}_{\mathrm{op}}\left(\frac{64}{3}N_f-\frac{32}{3}+104\right).
\end{aligned} \tag{B9}
$$

For the WFF, the enhancement process requires computing the 2D WFT of the input image, then threshold the coefficients and apply the inverse 2D WFT. When computing the 2D WFT, 2D convolution is performed for all frequency samples in horizontal and vertical directions, which count N_{wx} and N_{wy} in total, respectively. It is realized by using a fast FT (FFT), the complexity of which is given by

$$
\begin{aligned}
C_{\mathrm{2D-WFT}}(N,M,N_{wx},N_{wy}) &\approx C_{\mathrm{FFT}} \\
&\quad + N_{wx}N_{wy}(C_{\mathrm{FFT}} \\
&\quad + NMC_{\mathrm{zmult}} + C_{\mathrm{IFFT}}),
\end{aligned} \tag{B10}
$$

where we denote C_{FFT} as the complexity for computing a $N\times M$ 2D FFT. Assume that the split-radix FFT [29,30] is adopted for its realization. Hence, $C_{\mathrm{FFT}} = C_{\mathrm{IFFT}} = (4\,MN\lg(MN) - 12\,MN + 8(M+N))C_{\mathrm{op}}$, where we count each complex multiplication as requiring four real multiplications and two real additions for its implementation and we denote $\lg(\cdot)$ as $\log_2(\cdot)$. There are $C_{\mathrm{WFF\text{-}thresh}} = N_{wx}N_{wy}\mathrm{NMC}_{\mathrm{thresh}}$ operations for the thresholding of 2D WFT coefficients. The complexity of the inverse WFT is given by

$$
\begin{aligned}
C_{\mathrm{2D-IWFT}}(N,M,N_{wx},N_{wy}) &\approx N_{wx}N_{wy}(C_{\mathrm{FFT}} \\
&\quad + \mathrm{NMC}_{\mathrm{zmult}} + C_{\mathrm{IFFT}}) \\
&\quad + (N_{wx}N_{wy}-1)\mathrm{NMC}_{\mathrm{add}}.
\end{aligned} \tag{B11}
$$

Therefore, the complexity of the WFF algorithm is

$$
\begin{aligned}
C_{\mathrm{WFF}} &= C_{\mathrm{2D-WFT}}(N,M,N_{wx},N_{wy}) \\
&\quad + C_{\mathrm{2D-IWFT}}(N,M,N_{wx},N_{wy}) + C_{\mathrm{WFF-thresh}} \\
&= C_{\mathrm{op}}(1+4N_{wx}N_{wy})(4NM\lg(NM) - 12NM \\
&\quad + 8(M+N)) + C_{\mathrm{op}}NM(14N_{wx}N_{wy}-1).
\end{aligned} \tag{B12}
$$

To guarantee stable enhancement results, the number of frequency samples must be sufficient. In practice, for a 512 pixel × 512 pixel image with carrier cycle of about 8 pixels, if we select $N_{wx} = N_{wy} > 20$, the quality of the enhanced fringe image will be comparable to that of the proposed algorithm.

This work is supported by the Hong Kong Polytechnic University (grant G-U518).

References

1. S. Zhang and S. T. Yau, "High-speed three-dimensional shape measurement system using a modified two-plus-one phase-shifting algorithm," Opt. Eng. **46**, 113603 (2007).
2. T. W. Hui and G. K. H. Pang, "3-D measurement of solder paste using two-step phase shift profilometry," IEEE Trans. Electron. Packag. Manufact. **31**, 306–315 (2008).
3. X. Su and W. Chen, "Fourier transform profilometry: A review," Opt. Lasers Eng. **35**, 263–284 (2001).
4. M. Takeda and K. Mutoh, "Fourier transform profilometry for the automatic measurement of 3-D object shapes," Appl. Opt. **22**, 3977–3982 (1983).
5. J. Zhong and J. Weng, "Spatial carrier-fringe pattern analysis by means of wavelet transform: Wavelet transform profilometry," Appl. Opt. **43**, 4993–4998 (2004).

6. J. Zhong and J. Weng, "Phase retrieval of optical fringe patterns from the ridge of a wavelet transform," Opt. Lett. **30**, 2560–2562 (2005).
7. M. A. Gdeisat, D. R. Burton, and M. J. Lalor, "Spatial carrier fringe pattern demodulation by use of a two-dimensional continuous wavelet transform," Appl. Opt. **45**, 8722–8732 (2006).
8. S. Li, X. Su, and W. J. Chen, "Spatial carrier fringe pattern phase demodulation by use of a two-dimensional real wavelet," Appl. Opt. **48**, 6893–6906 (2009).
9. D. C. Ghiglia and M. D. Pritt, *Two-Dimensional Phase Unwrapping: Theory, Algorithms, and Software* (Wiley, 1998).
10. J. Bioucas-Dias and G. Valadao, "Phase unwrapping via graph cuts," IEEE Trans. Image Process. **16**, 698–709 (2007).
11. J. S. Lee, K. P. Papathanassiou, T. L. Ainsworth, M. R. Grunes, and A. Reigber, "A new technique for noise filtering of SAR interferometric phase images," IEEE Trans. Geosci. Remote Sens. **36**, 1456–1465 (1998).
12. C. Lopez-Martinez and X. Fabregas, "Modeling and reduction of SAR interferometric phase noise in the wavelet domain," IEEE Trans. Geosci. Remote Sens. **40**, 2553–2566 (2002).
13. J. Bioucas-Dias, V. Katkovnik, J. Astola, and K. Egiazarian, "Absolute phase estimation: Adaptive local denoising and global unwrapping," Appl. Opt. **47**, 5358–5369 (2008).
14. V. Katkovnik, J. Astola, and K. Egiazarian, "Phase local approximation (PhaseLa) technique for phase unwrap from noisy data," IEEE Trans. Image Process. **17**, 833–846 (2008).
15. K. Qian, "Windowed Fourier transform for fringe pattern analysis," Appl. Opt. **43**, 2695–2702 (2004).
16. K. Qian, "Windowed Fourier transform for fringe pattern analysis: Addendum," Appl. Opt. **43**, 3472–3473 (2004).
17. K. Qian, "Windowed Fourier transform for fringe pattern analysis: Principles, applications and implementations," Opt. Lasers Eng. **45**, 304–317 (2007).
18. K. Qian, H. N. Le Tran, F. Lin, and H. S. Seah, "Comparative analysis on some filters for wrapped phase maps," Appl. Opt. **46**, 7412–7418 (2007).
19. L. Huang, Q. Kemao, B. Pan, and A. K. Asundi, "Comparison of Fourier transform, windowed Fourier transform, and wavelet transform methods for phase extraction from a single fringe pattern in fringe projection profilometry," Opt. Lasers Eng. **48**, 141–148 (2010).
20. I. Daubechies, M. Defrise, and C. D. Mol, "An iterative thresholding algorithm for linear inverse problems with a sparsity constraint," Commun. Pure Appl. Math. **57**, pp. 1413–1457 (2004).
21. M. Elad, "Why simple shrinkage is still relevant for redundant representations?" IEEE Trans. Inf. Theory **52**, 5559–5569 (2006).
22. M. Elad, B. Matalon, and M. Zibulevsky, "Image denoising with shrinkage and redundant representations," *2006 IEEE Computer Society Conference on Computer Vision and Pattern Recognition* (IEEE, 2006), Vol. 2, pp. 1924–1931.
23. J. M. Bioucas-Dias and M. A. T. Figueiredo, "A new TwIST: Two-step iterative shrinkage/thresholding algorithms for image restoration," IEEE Trans. Image Process. **16**, 2992–3004 (2007).
24. A. M. Bruckstein, D. L. Donoho, and M. Elad, "From sparse solutions of systems of equations to sparse modeling of signals and images," SIAM Rev. **51**, 34–81 (2009).
25. I. W. Selesnick, R. G. Baraniuk, and N. G. Kingsbury, "The dual-tree complex wavelet transform," IEEE Signal Process. 123–151 (2005).
26. H. Shi, B. Hu, and J. Q. Zhang, "A novel scheme for the design of approximate Hilbert transform pairs of orthonormal wavelet bases," IEEE Trans. Signal Process. **56**, 2289–2297 (2008).
27. D. L. Donoho and I. M. Johnstone, "Adapting to unknown smoothness via wavelet shrinkage," J. Am. Stat. Assoc. **90**, 1200–1224 (1995).
28. S. G. Mallat, *A Wavelet Tour of Signal Processing* (Academic, 1999).
29. P. Duhamel and H. Hollmann, "'Split radix' FFT algorithm," Electron. Lett. **20**, 14–16 (1984).
30. S. G. Johnson and M. Frigo, "A modified split-radix FFT with fewer arithmetic operations," IEEE Trans. Signal Process. **55**, 111–119 (2007).